


RESEARCH ARTICLE | DECEMBER 06 2022

LES investigation into the cavity shedding dynamics and cavitation–vortex interaction around a surface-piercing hydrofoil

Yuchang Zhi (支玉昌); Renfang Huang (黄仁芳) ; Rundi Qiu (丘润荻); ... et. al



Physics of Fluids 34, 123314 (2022)

<https://doi.org/10.1063/5.0123381>



View
Online



Export
Citation

CrossMark

Articles You May Be Interested In

Investigation of unsteady cryogenic cavitating flow and induced noise around a three-dimensional hydrofoil

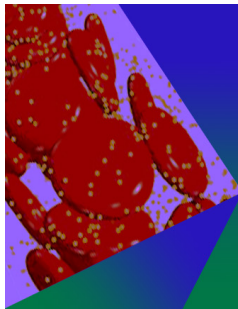
Physics of Fluids (April 2022)

Dynamic response and acoustic characteristics of composite hydrofoil under cavitation-induced vibration

Physics of Fluids (January 2023)

Physical investigation of transient dynamic behaviors of cavitation-induced vibration over a flexible hydrofoil

Physics of Fluids (November 2021)



Physics of Fluids

Special Topic: Flow and Forensics

Submit Today!

 AIP
Publishing

 AIP
Publishing

LES investigation into the cavity shedding dynamics and cavitation–vortex interaction around a surface-piercing hydrofoil

Cite as: Phys. Fluids **34**, 123314 (2022); doi: 10.1063/5.0123381
Submitted: 30 August 2022 · Accepted: 16 November 2022 ·
Published Online: 6 December 2022



View Online



Export Citation



CrossMark

Yuchang Zhi (支玉昌),¹  Renfang Huang (黄仁芳),^{2,a)}  Rundi Qiu (丘润荻),^{2,3} Yiwei Wang (王一伟),^{2,3,4,a)} 
and Chenguang Huang (黄晨光)^{2,3,4} 

AFFILIATIONS

¹School of Aeronautics and Astronautics, Sun Yat-Sen University, Guangzhou 510275, China

²Key Laboratory for Mechanics in Fluid Solid Coupling Systems, Institute of Mechanics, Chinese Academy of Sciences, Beijing 100190, China

³School of Future Technology, University of Chinese Academy of Sciences, Beijing 100049, China

⁴School of Engineering Science, University of Chinese Academy of Sciences, Beijing 100049, China

Note: This paper is part of the special topic, Cavitation.

^{a)} Authors to whom correspondence should be addressed: hrenfang@imech.ac.cn and wangyw@imech.ac.cn

ABSTRACT

Recent experiments have found that there is unstable vaporous cavitation around a surface-piercing hydrofoil at high Froude numbers and small yaw angles, and it would promote ventilation formation [R. Huang *et al.*, “Investigations into the ventilated cavities around a surface-piercing hydrofoil at high Froude numbers,” Phys. Fluids **34**, 043304 (2022)], but the cavity shedding dynamics and the mechanism of cavitation–vortex interaction are still open problems. In this paper, the unstable vaporous cavities around a surface-piercing hydrofoil are numerically investigated using the large-eddy simulation coupled with the Schnerr–Sauer cavitation model. Numerical simulations can predict the cavity features, including an aerated base cavity aft of the hydrofoil trailing edge, vaporous cavitation at the hydrofoil suction surface, and tip–vortex cavitation. A U-shaped vapor cloud shedding together with a horseshoe vortex is observed during the unsteady cavitation evolution, that is, the cavity development, cutoff, and collapse. This irregular shedding is related to the three-dimensional reentrant jet induced by the velocity reflection at the vaporous cavity closure line. Furthermore, the effects of the vaporous cavitation on the vorticity generation are attributed to vortex stretching, baroclinic torque, and vortex dilatation by using the vorticity transport equation. This study could contribute to the novel hydrofoil designs and their flow control.

Published under an exclusive license by AIP Publishing. <https://doi.org/10.1063/5.0123381>

I. INTRODUCTION

The hydrofoil is an important component of the hydrofoil craft to provide lift. However, when the hydrofoil undergoes cavitation,^{2,3} that is, the phase transition from liquid water to vaporous water cavitation will cause a significant drop in the hydrofoil lift and the cavitation instability will affect the hydrodynamic stability of the hydrofoil.^{3,4} Thus, studying the cavitation stability of the surface-piercing hydrofoil is crucial for the hydrodynamic design of marine vehicles. This paper focuses on the vaporous cavitation around the surface-piercing hydrofoil, rather than the atmospheric ventilation.

It is widely acknowledged that the cavitating flow around a hydrofoil has inherent unsteady characteristics.^{5–9} Many scholars have conducted extensive research on the three-dimensional hydrofoil

through numerical calculations^{10,11} and experimental measurements.^{12–16} The quasi-periodic vaporous cavity shedding^{10,11} is observed in the cavitation tunnel. It is proved that the vaporous cavity break-off and shedding are related to the reentrant jet on account of the inverse pressure gradient. Foeth *et al.*^{12,13} investigated the vaporous cavity evolution over a twisted hydrofoil by using particle image velocimetry. The results show that the primary shedding is determined by the reentrant jet, and the secondary shedding is attributed to the side entrant jet. De Lange and De Bruin¹⁴ performed cavitation experiments for a hydrofoil. According to their results, the reentrant jet has three-dimensional characteristics and it would mirror at the cavity closure line. Peng *et al.*¹⁵ conducted a series of experiments on different hydrofoils, and the results showed that U-shaped flow structures are

common in cloud cavities and shedding is mainly caused by reentrant flow. Kawanami *et al.*¹⁶ used a high-speed camera to study the mechanism of cloud cavitation and measured the shedding frequency and cavitation scale of cavitation shedding.

Numerical simulation is considered to be an effective approach to obtaining the coherent structures of unsteady cavitating flow around a hydrofoil.^{17,18} A large number of numerical calculations demonstrate that numerical simulation can well capture the cavity shedding behaviors as observed in the experiments, and the calculation results can directly illustrate the intricate cavitating flow fields and multiscale vortex structures.^{19–21} Ji *et al.*^{22–25} carried out a range of numerical studies about unstable vortical cavitation around the twisted hydrofoil. Their investigations show that the primary U-shaped shedding is formed when the radially diverging reentrant jet collides with the closure surface of the attached cavity, and two secondary U-shaped vapor clouds are generated when the radially diverging reentrant jet collides with the side-entrant jets.²⁵ Large-scale coherent structures during the cavitation evolution were studied by using proper orthogonal decomposition,²⁶ and the dominant and harmonic frequencies were predicted well when compared with the experimental values.²⁷

Limited previous reports about cavitation near the free surface demonstrate that the free surface would affect the cavity dynamic behaviors when the immersed depth of the blunt body or hydrofoil is the same order of magnitude as its characteristic size.^{28–30} Xu *et al.*³¹ performed experiments and calculations of the cloud cavitation process over a hydrofoil, which was influenced by the free surface. Based on their results, the cavity is asymmetric near the free surface and the cavity evolution process includes three stages, that is, cavity inception, development, shedding, and collapse.³¹ Wang *et al.*^{32,33} and Xu *et al.*^{34–36} also carried out a range of experiments and numerical simulations of the unsteady cavitation features around a blunt body, which was launched near the free surface. The results show that cavitation is more seriously affected by the free surface, such as the cavity length, and cavity collapse strength, when the immersed depth becomes smaller.

Influenced by the free surface, the hydrodynamic behaviors of a surface-piercing hydrofoil are very complex, which can induce gas ventilation and vaporous cavitation.^{37–43} The vaporous cavitating flow over the surface-piercing plate hydrofoil is typically three-dimensional when compared with the cavitation around a fully submerged hydrofoil. Waid⁴³ conducted ventilation experiments at high Froude numbers and small cavitation numbers using a strut in a depressurized tank, indicating that the vaporous cavity near the suction surface (SS) of an underwater strut is unstable and exhibits periodic shedding due to the reentrant jet. Huang *et al.*¹ carried out many experiments on a plate hydrofoil at high Froude numbers and also observed unstable vaporous cavitation at very high Froude numbers, presenting with cavity growth, destabilization, and collapse. Harwood *et al.*^{44,45} found that the instabilities of ventilated cavities depend on the three-dimensional reentrant jet for a surface-piercing hydrofoil in experiments. Zhi *et al.*⁴⁶ numerically confirmed that the reentrant jets are crucial to maintaining the ventilated cavity stability. Wang *et al.*⁴⁷ showed the interaction mechanism between supercavitation and ventilated cavities. Their results demonstrate that the numerical simulation could accurately describe the ventilated cavitation evolution.

Based on the literature review, the multiphase flow over a surface-piercing plate hydrofoil is studied by experiments or numerical simulations. On the one hand, the ventilated cavity and the vaporous cavity can be observed experimentally, but it is difficult to illustrate the internal flow details. On the other hand, most numerical simulations focus on the low-speed operating conditions and only investigate the ventilated cavity without considering the vaporous cavitation at high speeds. All in all, there are a few kinds of literature exploring the cavitation shedding dynamics and the cavitation–vortex interaction mechanism for a surface-piercing hydrofoil at high speeds, and the free surface influence is still not clear.

Therefore, this study further extends the knowledge of vaporous cavitation mechanisms around a surface-piercing hydrofoil at a small yaw angle and high Froude number. The unsteady vaporous cavitation characteristics are captured by the numerical simulation. Then, an in-depth analysis of the unsteady three-dimensional cavitating flow is conducted, focusing on the interaction mechanism between the vortex motion and cavitation development, and the three-dimensional effect of the reentrant jet.

II. NUMERICAL METHODS

A. Governing equations

When the plate hydrofoil is piercing the water at high speeds, it involves three phases, that is, air, vapor, and liquid water.^{41–43,48} In this paper, the multiphase fluid components are treated as one-fluid flow; that is, each fluid component shares the same pressure and velocity fields.⁴⁹ Therefore, the governing equations are written as

$$\frac{\partial \rho}{\partial t} + \frac{\partial(\rho u_i)}{\partial x_i} = 0, \tag{1}$$

$$\frac{\partial(\rho u_i)}{\partial t} + \frac{\partial(\rho u_i u_j)}{\partial x_j} = -\frac{\partial p}{\partial x_i} + \frac{\partial}{\partial x_j} \left(\mu \frac{\partial u_i}{\partial x_j} \right), \tag{2}$$

where μ denotes the viscosity, p denotes the pressure, ρ denotes the mixture density for multiphase flow, and u_i denotes the velocity component in the i th direction.

The volume-of-fluid (VOF) method⁵⁰ is adopted to capture interfaces among the immiscible phases. The phase distribution and the interface position are described by the volume fraction (α) of phase n ,

$$\alpha_n = \frac{V_n}{V}, \tag{3}$$

where V_n represents the volume of n th phase within the cell, $n = 1-3$, and V indicates the volume of the cell. Note that the sum of the volume fraction for each phase in a cell should satisfy the following constraint:

$$\alpha_l + \alpha_g + \alpha_v = 1, \tag{4}$$

where subscripts l , g , and v correspond to the liquid, air, and vapor, respectively.

The mixture density ρ and the mixture viscosity μ can be defined as a volume-weighted average of the three components, which can be written as

$$\rho = \alpha_l \rho_l + \alpha_v \rho_v + (1 - \alpha_v - \alpha_l) \rho_g, \tag{5}$$

$$\mu = \alpha_l \mu_l + \alpha_v \mu_v + (1 - \alpha_v - \alpha_l) \mu_g, \tag{6}$$

where $\mu_l = 1.003 \times 10^{-3}$, $\mu_v = 1.340 \times 10^{-5}$, and $\mu_g = 1.789 \times 10^{-5}$ Pa·s are the viscosities of the water liquid, vapor, and air, respectively. $\rho_l = 998.2$, $\rho_v = 0.5542$, and $\rho_g = 1.225 \text{ kg/m}^3$ are the densities of the water liquid, vapor, and air, respectively. α_v and α_g are dominated by the mass transport equations

$$\frac{\partial(\rho_v \alpha_v)}{\partial t} + \frac{\partial(\rho_v \alpha_v u_j)}{\partial x_j} = \dot{m}^+ - \dot{m}^-, \quad (7)$$

$$\frac{\partial(\rho_g \alpha_g)}{\partial t} + \frac{\partial(\rho_g \alpha_g u_j)}{\partial x_j} = 0, \quad (8)$$

where \dot{m}^+ and \dot{m}^- are the source terms, representing the evaporation and condensation during the phase transition,⁵¹ which are closed by the Schnerr–Sauer cavitation model in Eqs. (9) and (10),⁵²

$$\dot{m}^+ = \frac{\rho_v \rho_l}{\rho} \alpha_v (1 - \alpha_v) \frac{3}{R_b} \sqrt{\frac{2 \max(p_v - p, 0)}{3 \rho_l}}, \quad (9)$$

$$\dot{m}^- = \frac{\rho_v \rho_l}{\rho} \alpha_v (1 - \alpha_v) \frac{3}{R_b} \sqrt{\frac{2 \max(p - p_v, 0)}{3 \rho_l}}, \quad (10)$$

where the saturated vapor pressure is $p_v = 3169$ Pa, R_b is the bubble radius, and the relationship between R_b and α_v is defined in Eq. (9).

$$R_b = \left(\frac{\alpha_v}{1 - \alpha_v} \frac{3}{4\pi N_b} \right)^{\frac{1}{3}}, \quad (11)$$

where N_b is the number density of bubbles, and we set $N_b = 10^{13}$, which could predict the unsteady cavitation well based on previous studies.^{11,53}

B. Large-eddy simulation (LES) approach

Large-eddy simulation (LES) approach is adopted to solve the governing equations so that the large-scale coherent structures can be directly resolved and the small-scale coherent structures are modeled by a sub-grid-scale (SGS) model.⁵⁴ Applying a Favre-filtering operation to Eqs. (1) and (2), we can obtain

$$\frac{\partial \rho}{\partial t} + \frac{\partial \rho \bar{u}_j}{\partial x_j} = 0, \quad (12)$$

$$\frac{\partial(\rho \bar{u}_i)}{\partial t} + \frac{\partial(\rho \bar{u}_i \bar{u}_j)}{\partial x_j} = -\frac{\partial \bar{p}}{\partial x_i} + \frac{\partial}{\partial x_j} \left(\mu \frac{\partial \bar{u}_i}{\partial x_j} \right) - \frac{\partial \tau_{ij}}{\partial x_j}, \quad (13)$$

where the overbars represent the filtered quantities, and τ_{ij} represents the sub-grid-scale (SGS) stress with the definition in Eq. (14)

$$\tau_{ij} = \rho(\bar{u}_i \bar{u}_j - \bar{u}_i \bar{u}_j). \quad (14)$$

The SGS stress is modeled by the Smagorinsky model, where it is assumed that the SGS stresses are proportional to the modulus of the strain rate tensor, \bar{S}_{ij} , of the filtered large-scale flow. The SGS stress is regarded as

$$\tau_{ij} - \frac{1}{3} \tau_{kk} \delta_{ij} = -2\mu_t \bar{S}_{ij}. \quad (15)$$

In Eq. (15), \bar{S}_{ij} represents the strain rate tensor for the resolved quantities, μ_t represents the SGS turbulent viscosity, and τ_{kk} represents the isotropic part.

A wall adapting local eddy-viscosity (WALE) model⁵⁵ is adopted to closure the SGS μ_t . The detailed mathematical formula is defined as follows:

$$\mu_t = \rho \Delta_s^2 \frac{(S_{ij}^d S_{ij}^d)^{3/2}}{(\bar{S}_{ij} \bar{S}_{ij})^{5/2} + (S_{ij}^d S_{ij}^d)^{5/4}}, \quad (16)$$

$$\bar{S}_{ij} = \frac{1}{2} \left(\frac{\partial \bar{u}_i}{\partial x_j} + \frac{\partial \bar{u}_j}{\partial x_i} \right), \quad (17)$$

$$S_{ij}^d = \frac{1}{2} (\bar{g}_{ij}^2 + \bar{g}_{ji}^2) - \frac{1}{3} \delta_{ij} \bar{g}_{kk}^2, \quad (18)$$

$$\bar{g}_{ij} = \frac{\partial \bar{u}_i}{\partial x_j}. \quad (19)$$

Δ_s in Eq. (16) is the mixing length of the SGS model, which is calculated by

$$\Delta_s = \min(\kappa d, C_s V^{1/3}), \quad (20)$$

where V represents the grid cell volume, κ represents the von Karman constant, C_s represents a WALE model parameter with the default value of 0.5, and d represents the shortest distance to the solid wall.

C. Wave damping

Wave damping is performed on the outlet and side boundaries of the computational domain to prevent the reflection of the free surface wave, which can be achieved by introducing resistance to vertical motion. The method⁵⁶ is to add a resistance term to the equation for w -velocity:

$$S_z^d = \rho(f_1 + f_2 |w|) \frac{e^{\xi} - 1}{e^1 - 1} w \quad (21)$$

with

$$\xi = \left(\frac{x - x_{sd}}{x_{ed} - x_{sd}} \right)^{n_d}, \quad (22)$$

where x_{sd} is the starting point for wave damping (propagation in the x direction); x_{ed} is the end point for wave damping (boundary); f_1 , f_2 , and n_d are parameters of the damping model; and w is the vertical velocity component.

III. NUMERICAL SETUP

A. Hydrofoil geometry and boundary conditions

A symmetrical plate hydrofoil¹ is treated in this study, as shown in Fig. 1. Geometric parameters and operation condition of the hydrofoil are listed in Table I. The plate hydrofoil has an isosceles triangular cross section, where the hydrofoil chord length is $c = 0.05$ m and the vertex angle is 20° . The span of this plate hydrofoil is $S = 0.15$ m.¹ The base point of the coordinate system is set at the intersection point of the free surface and the hydrofoil leading edge (LE). Unsteady cavities for the plate hydrofoil piercing the free surface are extensively studied by Huang *et al.*¹ in a constrained-launching tank. This study focuses on the vaporous cavitation behaviors around this surface-piercing hydrofoil at high Froude numbers. Therefore, the calculation condition is as follows: the tip immersed depth is $h = 0.05$ m, the hydrofoil yaw angle is $\alpha_0 = 7.5^\circ$, the velocity is $u_h = 25$ m/s, corresponding to

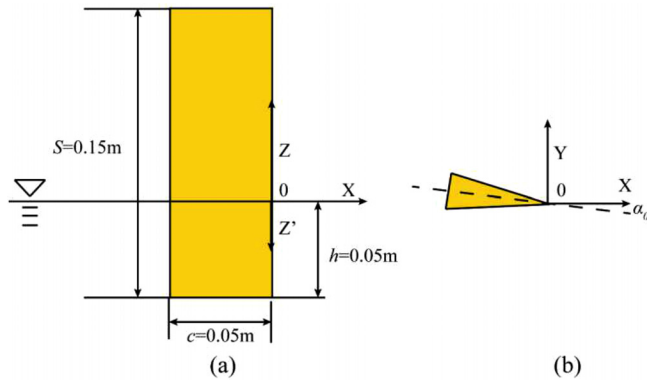


FIG. 1. Geometric model of the plate hydrofoil for the numerical calculation. (a) Hydrofoil dimensions and coordinate system, (b) cross section of the hydrofoil.

TABLE I. Geometric parameters and operation condition of the hydrofoil.

Parameter	Symbol	Value
Hydrofoil chord length (m)	c	0.05
Hydrofoil span (m)	S	0.15
Immersed depth of the foil tip (m)	h	0.05
Immersed aspect ratio	$AR_h = \frac{h}{c}$	1.0
Yaw angle ($^\circ$)	α_0	7.5
Velocity (m/s)	u_h	25
Depth Froude number	$Fr_h = \frac{u_h}{\sqrt{gh}}$	35.71
Vaporous cavitation number	$\sigma = (p_{out} - p_v)/(0.5\rho_l u_h^2)$	0.32

the depth Froude number $Fr_h = 35.71$, and cavitation number $\sigma = 0.32$.

Boundary conditions and computational domain⁴⁶ for multi-phase cavities around the surface-piercing hydrofoil are presented in Fig. 2. To prevent the reflected waves from affecting the calculation accuracy, the computational domain must be large enough to keep the boundaries away from the hydrofoil.⁵⁷ On the one hand, the hydrofoil is situated in a cuboid with a height of $15c$, a width of $10c$, and a length of $30c$. The inlet of the computational domain is $10c$ upstream of the hydrofoil leading edge (LE), and the outlet is $20c$ downstream of the

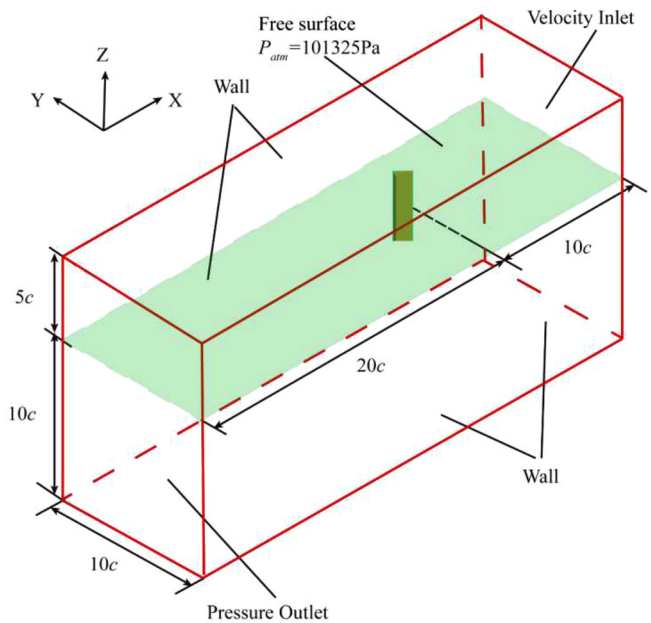


FIG. 2. Computational domain with boundary condition settings.

hydrofoil LE. The lower surface of the computational domain is $10c$ below the free surface, and the upper surface is $5c$ above the free surface. On the other hand, the wave damping zone is $2c$ long and it is set near the outlet and lateral walls to prevent reflected waves from affecting the flow around the hydrofoil, as shown in Fig. 3. A uniform inflow condition is prescribed at the inlet boundary, the incoming velocity is specified as $u_h = 25$ m/s at the inlet, and the turbulence intensity is 0 at the inlet. The pressure outlet is set as a hydrostatic pressure distribution of a flat VOF wave based on the water–gas component. Free surface pressure is a standard atmospheric pressure, with $P_{atm} = 101\,325$ Pa. The hydrofoil surface and all the other boundaries are set as no-slip walls.

The numerical simulations are carried out using the commercial CFD software STAR-CCM+ 13.06. The unsteady governing equations are iteratively solved by using the SIMPLE algorithm. The spatial term is discretized using the second-order upwind scheme, the temporal term is discretized using the second-order implicit scheme, and a central difference method is utilized for the convection term.

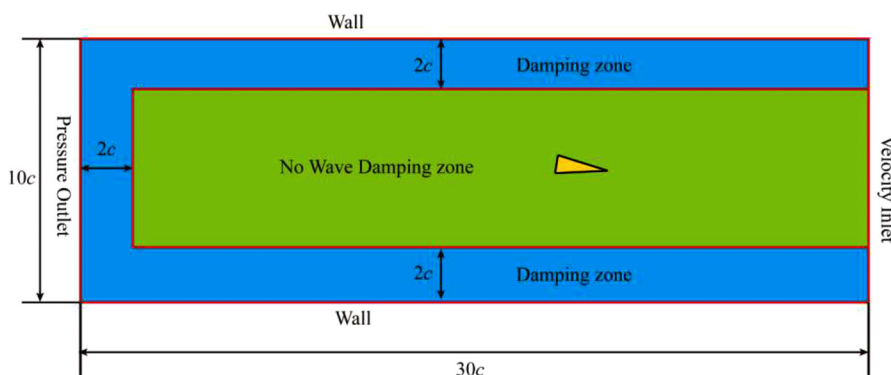


FIG. 3. Top view of wave damping zone.

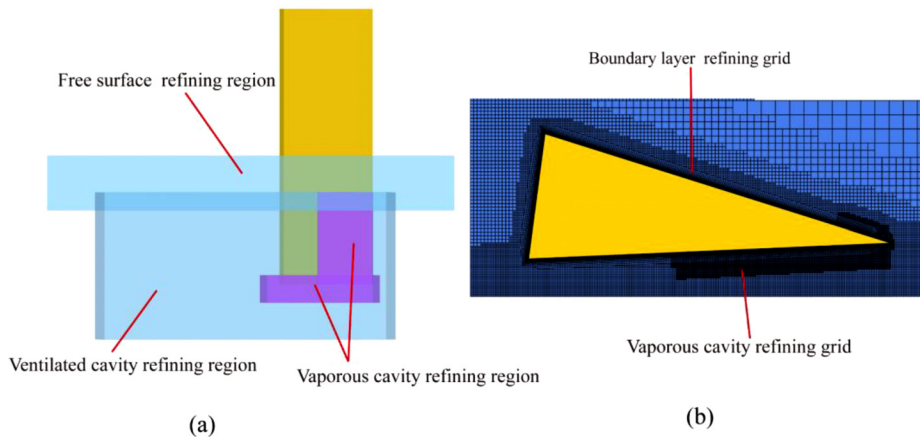


FIG. 4. Meshing details. (a) Refining regions, (b) local refining grids.

The high-resolution interface capturing (HRIC) scheme²⁹ is employed for the VOF solution due to its advantage in tracking the sharp interfaces between the two immiscible phases. The time step is set as $\Delta t = T_{ref}/400 = 5 \times 10^{-6}$ s, where $T_{ref} = c/u_h$, as suggested by Coutier-Delgosha *et al.*^{58,59} This numerical approach has been used to study many similar cases,^{29,31–36} such as hydrofoil or projectile near free surface, so the cavity patterns and the effects of the free surface can be well captured by the present numerical approach when compared to the experiments.

B. Mesh details and verification

The grid is generated by the Cartesian grid method, and grid details around the surface-piercing hydrofoil are depicted in Fig. 4. Mesh refinement is conducted to enhance the calculation accuracy of the cavitating region and interfaces. Three refining regions are presented in Fig. 4(a), that is, the refining regions near the free surface, ventilated cavity, and vaporous cavity. First, surface remesher is performed on the hydrofoil surface; then, the high-quality surface mesh with good surface triangulation is generated. Finally, the volume meshes with prism layer mesh and trimmed mesh are generated based on the surface mesh. As for the mesh along the wall, the boundary layer was set to 32 layers with the boundary layer growth rate of 1.2, and the total thickness of the boundary layer was set to 0.0015 m. As suggested by Ji *et al.*,¹¹ we guarantee that y^+ near the hydrofoil wall is always less than 1 to meet the LES requirements for the grid resolution.

The discretization uncertainty is estimated by using the Richardson extrapolation method with three grids. Here, M represents 1×10^6 . The mesh refinement ratio is $r = N_2/N_1 = N_3/N_2 = 2$, where N_1 , N_2 , and N_3 are the number of cells for the coarse, medium, and fine meshes, respectively. Then, numerical verification is conducted at the condition, $u_h = 25$ m/s, $AR_h = 1$, $\alpha_0 = 7.5^\circ$, and the mean lift coefficient (\bar{C}_L) is treated as the solution, as defined in Eq. (23). Therefore, the corresponding solutions for these three sets of grids are f_1, f_2 , and f_3 , respectively,

$$\bar{C}_L = \frac{L}{0.5\rho u_h^2 hc}. \tag{23}$$

The grid convergence index (GCI)^{60,61} methods are used to check the grid independence, and it can be defined as

$$GCI_{32} = \frac{F_S |\epsilon_{32}|}{r^\gamma - 1}, \tag{24}$$

where F_S represents the safety factor with the recommended value of $F_S = 1.25$, and ϵ_{32} is the solution variation of the fine grid relative to the medium grid, that is, $\epsilon_{32} = f_3 - f_2$. γ is the order of convergence, which is calculated via Eq. (25).

$$\gamma = \ln \left(\frac{f_3 - f_2}{f_2 - f_1} \right) / \ln r. \tag{25}$$

Table II shows the grid convergence analysis based on the mean lift coefficient (\bar{C}_L). The \bar{C}_L error of the medium grid relative to the coarse grid is 0.27%, and the error of the fine grid relative to the medium grid is 0.75%, indicating the predicted accuracy for the three sets of meshes is very close. In addition, the grid convergence index for the medium and coarse meshes is $GCI_{21} = 0.18\%$, and it is 0.51% for the fine and medium meshes. It is worth noting that $GCI_{32} \approx r^7 \cdot GCI_{21}$ proves that the solutions of the three meshes are within the asymptotic convergence range.

Flow features predicted by the three sets of meshes are shown in Fig. 5, where the vaporous cavity is identified with the $\alpha_v = 0.1$ isosurface in white color, and the ventilated cavity is visualized by the $\alpha_g = 0.5$ isosurface in blue color. It is illustrated that the cavity patterns are well captured, such as the base ventilation, the vaporous tip-vortex, and the turbulent shedding of the vaporous cavity. In addition, the free surface calculated by the three meshes is almost the same. Therefore, to balance the computational cost and computational accuracy, the medium mesh is used as the final mesh.

TABLE II. Grid convergence study.

	Mesh	Mesh cells	\bar{C}_L	$GCI\text{-}\bar{C}_L$	Error (%)
1	Coarse	8.65M	0.070 65
2	Medium	17.25M	0.070 46	$GCI_{21} = 0.18\%$	0.27%
3	Fine	35.17M	0.070 99	$GCI_{32} = 0.51\%$	0.75%

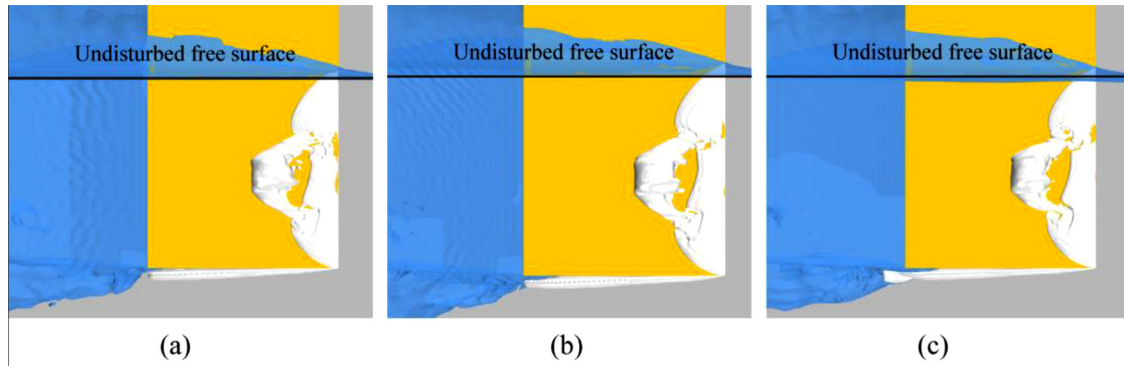


FIG. 5. Cavity patterns at a typical instant for: (a) numerical simulation via coarse mesh, (b) numerical simulation via medium mesh, (c) numerical simulation via fine mesh.

IV. RESULTS AND DISCUSSION

A. Unsteady sheet/cloud cavitation dynamics

The present simulation aims to analyze the shedding dynamics of unsteady vaporous cavitation over a surface-piercing plate hydrofoil. In our previous experiments,¹ the vaporous cavity is observed to go through a series of stages, that is, cavitation inception, growth, rolling up, shedding off, and finally collapse. The hydrofoil speed is not constant during the experiment. As the hydrofoil moves forward, the hydrofoil speed gradually decreases due to the water resistance, and thus, the vaporous cavity would disappear when its speed is reduced to a certain extent. In experiments, we observed two cycles of vaporous cavity shedding behaviors. Since the observation window is very small and the change of the hydrofoil speed is very small, it is assumed that the hydrofoil speed is constant in the numerical simulation. Numerical simulations were performed under $AR = 1$, $\alpha_0 = 7.5^\circ$, and $Fr_h = 35.71$, and a uniform inflow condition is prescribed at the inlet boundary. Compared with previous experimental results,¹ the vaporous cavity covers a greater area of the hydrofoil suction surface, and the dynamic behaviors of the vaporous cavity are pronounced. The cavity dynamic behavior of cavitation development/destabilization is also illustrated in the numerical calculation results.

To study the unsteady vaporous cavitation evolution predicted by the present numerical approach, the total vapor volume (V_{cav}) is monitored at each time step and it is defined in Eq. (26), where N_2 indicates the number of grid elements with the value of 17.25 M for the medium mesh based on the analysis in Sec. III. In Eq. (26), α_{vi} indicates the vapor volume fraction (α_v) of the i th grid cell, and V_i indicates the volume of the i th cell

$$V_{cav} = \sum_{i=1}^{N_2} \alpha_{vi} V_i. \tag{26}$$

Figure 6 shows the variations of the total vapor volume with time, and it depicts that the total vapor volume fluctuates periodically. Six instants are selected during one cycle to illustrate the time-dependent cavity evolution in Fig. 7, where the vaporous cavitation is identified via the $\alpha_v = 0.1$ isosurface in white color overlaid with the pressure contours at the hydrofoil suction side and ventilated cavities are visualized using the $\alpha_g = 0.5$ isosurface in blue color. In addition,

the corresponding velocity field at the midspan plane is depicted in the right column, superimposed with the cavity isosurface.

The vaporous cavity is attached to the hydrofoil, and the cavity length almost reaches its maximum with a convex shape in Fig. 7(a). Note that the cavity starts to become unstable since the pressure gradient is adverse at the vapor-liquid interface, which generates a reverse flow into the vaporous cavity. Therefore, the water and vapor are mixed, presenting white foamy water in the cavity rear, and the lateral sides (i.e., upper side and lower side) of the cavity are a single transparent medium. Subsequently, this reverse flow moves upstream, strikes at the incoming flow, and then cuts off the sheet cavity in Fig. 7(b), causing a primary shedding of the vaporous cavity at instant III [Fig. 7(c)]. This shedding cavity quickly rolls up into a turbulent vaporous cloud, corresponding to the maximum total cavity volume at instant III (Fig. 6). In Figs. 7(d) and 7(e), the shed cloud advects downstream through the main flow and shrinks along with high pressure. After that, the detached vapor cloud continues to move downstream and expands again in Fig. 7(f), accompanied by a slight increase in V_{cav} from instant V to instant VI as depicted in Fig. 6. Once the sheet cavity

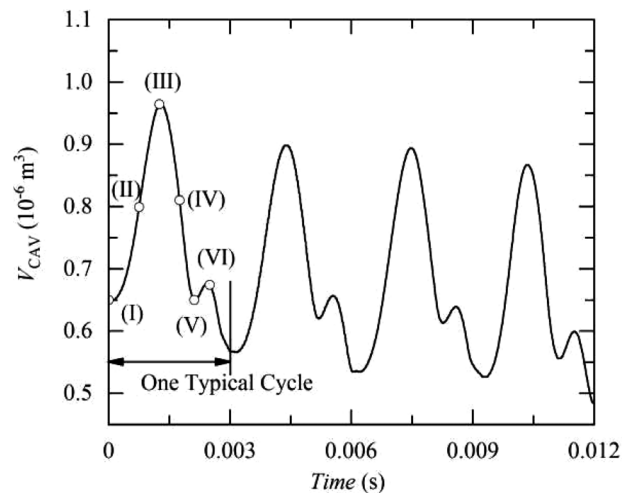


FIG. 6. The variations of the total vapor volume of the surface-piercing hydrofoil.

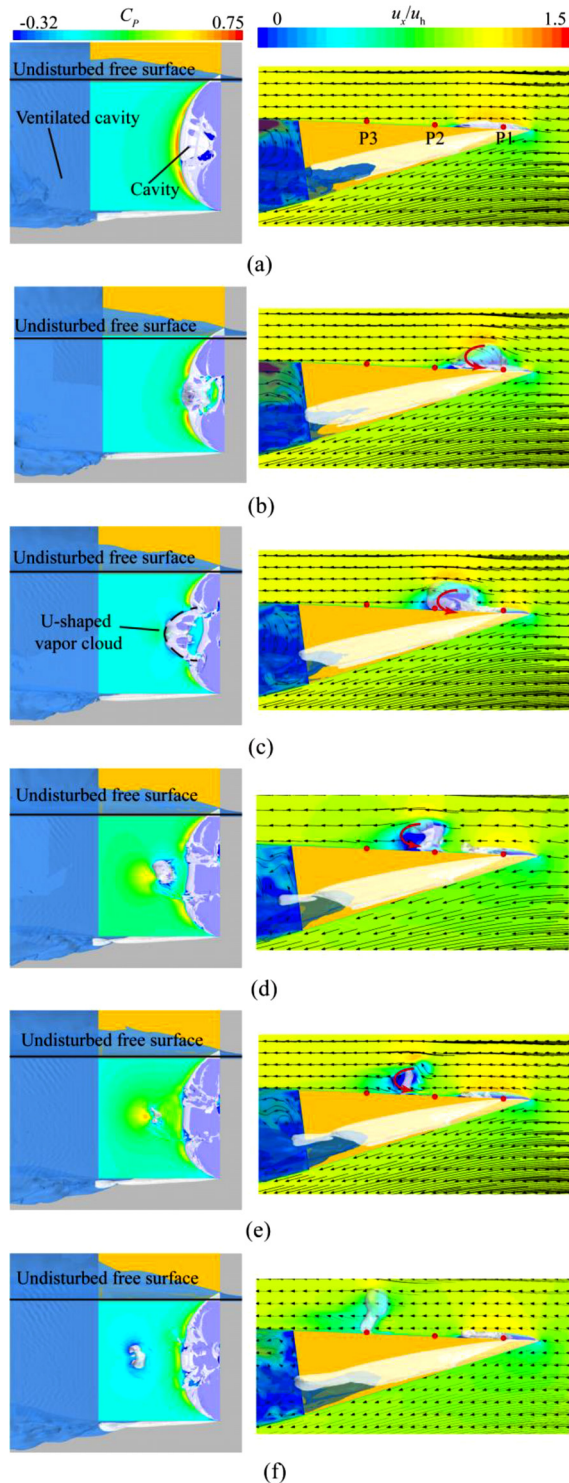


FIG. 7. Cavitation patterns during one typical cycle (Left: side view of the calculated result, Right: bottom view of the calculated data at the XY plane with $z = -0.025$ m). (a)–(f) corresponds to instant I–VI in Fig. 6. The positions of points P1–P3 are consistent with Fig. 9.

is cut off in Fig. 7(c), the residual cavity is concave. Subsequently, this cavity develops downstream into a new convex shape in Fig. 7(e), and then, it develops slowly in the streamwise direction.

In addition, it is worth noting that the cavity patterns generated by a surface-piercing hydrofoil are different from those in a cavitation tunnel.⁶² (1) A ventilated cavity (i.e., the air–liquid interface) is observed aft of the hydrofoil trailing edge (TE). This ventilated cavity is highly turbulent, presenting white foam in experiments, and it always exists during the unsteady vaporous cavitation evolution from the instant I to instant VI. (2) The free surface acts as a fluid film between the vaporous cavity and the ambient air, so the gas does not enter the vaporous cavity to form the tail ventilation. According to previous studies,^{41,63} this tail ventilation must be stimulated by the Taylor-type instabilities. (3) Interestingly, the primary shedding vapor cloud is U-shaped rather than two-dimensional. This is relevant to the 3D effect of the reentrant jet, which will be analyzed in the Sec. IV B. (4) An aerated base cavity is generated in the wake near the hydrofoil tip, and it tries industriously to develop upstream along the hydrofoil tip under the huge pressure difference. However, this aerated base cavity is restricted to a small region aft of the hydrofoil tip due to the strong scouring effect of the mainstream. In addition, the vaporous cavitation occurs at the tip–vortex due to the low pressure herein, but it does not intersect with the aerated base cavity, as illustrated in the right column of Fig. 7. As a result, there is no vapor–cavitation-induced ventilation.¹ Based on our previous study, this ventilation formation mechanism must occur at high Froude numbers and smaller yaw angles.¹

From Figs. 6 and 7, it is demonstrated that V_{cav} changes periodically with the unsteady cavity evolution for four typical cycles. Instant I–III represents the cavity shedding process. Instant III–V represents the advection and contraction of the shed vaporous cloud and the regrowth of the residual vaporous cavity. Instant V–VI represents the expansion of the shed vaporous cavity and the regrowth of the residual cavitation.

The time-dependent lift coefficient (C_L) of the plate hydrofoil is shown in Fig. 8. The lift coefficient changes very complicatedly with the unsteady cavitation evolution. Cavitation is a complex unsteady phenomenon that includes cavity shedding, shrinkage, expansion, and collapse. In Fig. 8, the variation of the lift coefficient is related to the variation of cavity coverage area during instant II–III and the cavity shrinkage during instant IV–V. For another, the regrowth of the attached cavity (during instant III–IV and instant V–VI) indicates that the low-pressure vaporous region becomes larger, and thus, the lift coefficient becomes larger. The time-averaged C_L is 0.070. It is noted that the pressure variation at each point is strongly affected by the cavitation evolution and the impact pressure generated by the cavity collapse. However, the lift force is the synthesis of the pressure distribution on the surface of the three-dimensional hydrofoil, and there is no strict one-to-one correspondence between the lift force and the cavitation evolution.

To analyze the effects of the unsteady cavity behaviors on the pressure pulsations, three monitoring points were selected at the hydrofoil SS. Points 1–3 are, respectively, located at $x/c = 0.1, 0.4,$ and 0.7 at the midspan of the hydrofoil submerged portion, as shown in Fig. 9. Point 1 is close to the hydrofoil LE, point 2 is a little bit outside the vaporous cavity at the instant I, and point 3 is far away from the cavitation region.

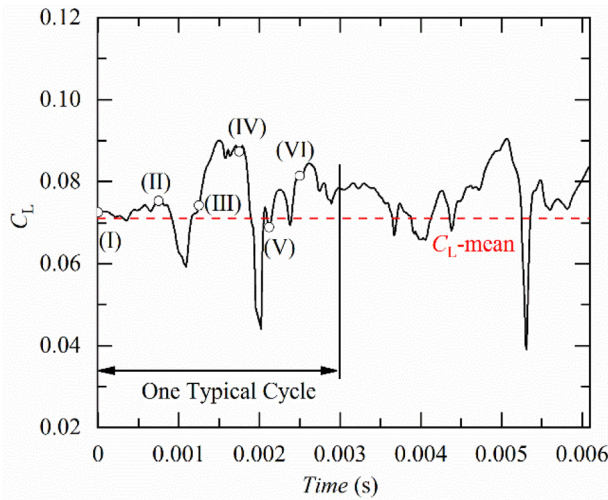


FIG. 8. Variations of the lift coefficient over time.

Figure 10(a) shows the pressure variation with time at the three monitoring points. It is indicated that the pressure at the suction surface varies intensely with the unsteady cavitation evolution. Point $x/c = 0.1$ is covered by the sheet cavity at instant I, so the local pressure is first at saturated vapor pressure. Subsequently, the pressure at point 1 starts to increase until instant II due to the cavity break-off, and then, it falls to the saturated vapor pressure when the residual cavity is regenerated again to cover point 1 (during instant III–VI). The pressure at point 2 gradually reduces to the saturated vapor pressure when the detached vapor cloud passes by (from instant II to instant IV), and after that, the pressure starts to rise. The shed vapor cloud has little effect on the pressure at point $x/c = 0.7$, but, interestingly, the pressure changes obviously from instant IV to instant VI. It is because the shrinkage of the shed cloud at instant V causes the pressure to increase, and its expansion at instant VI leads to the pressure reduction. This is also confirmed by the pressure variation in Figs. 7(d)–7(f). In addition, Fig. 10(b) depicts the power spectral density (PSD)⁶⁴ at the three monitoring points, where the sampling interval ΔT is 1×10^{-5} s, the number of samples L is 1800, and the frequency resolution is defined as $F_c = 1/\Delta T/L = 55.56$ Hz. The primary frequency of the unstable cavitation evolution for the surface-piercing hydrofoil is 332.963 Hz, which is much greater than the frequency resolution, and the corresponding cycle is 0.003 s, the Strouhal number $St = 0.666$,

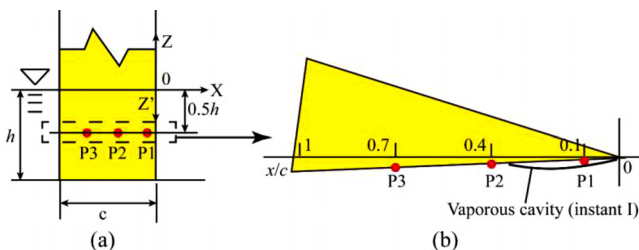


FIG. 9. Schematic diagram of the location of the three pressure monitoring points. (a) Global view, (b) partially enlarged view.

which belongs to a high-frequency event. The slope of the power spectral density is approximately $-5/3$ scaling, indicating the present LES approach can resolve to the inertial subrange and capture the turbulence spectrum.

B. Interpretation of the three-dimensional reentrant jet

The velocity distribution at the hydrofoil SS is depicted in Fig. 11 during one typical cycle, which is overlaid with the cavitation patterns. As stated in Sec. IV A, the vaporous cavitation only presents U-shaped shedding around the midspan part of the hydrofoil and the velocity distribution is three-dimensional along the foil span. Specifically, the velocity has the same direction as the mainstream around the shed vapor cloud, while it is opposite to the mainstream direction inside the vaporous cavity region. This is known as the reentrant jet, and it has an obvious three-dimensional effect as illustrated in Fig. 11, since the velocity is specularly reflected at the vaporous cavity closure line.^{14,65} The detailed interpretation is shown in Fig. 12. According to the Bernoulli equation of potential theory, we suppose that the multiphase flow is steady and the interior pressure inside the vaporous cavity is constant; then, the incoming velocity is reflected at the vapor–liquid interface. The incoming velocity can be decomposed into the normal component perpendicular to the cavity closure line and the tangential component tangent to the cavity closure line as depicted in Fig. 12(b). The reentrant jet is then obtained after the mirror-like reflection; that is, the tangential component is fixed and the direction of the normal component is inverted as depicted in Fig. 12(b). The fact that the tangential velocity is fixed can be derived from the momentum equation in this direction. As a result, on the one hand, at the cavity centerline, the reentrant jet and the incoming velocity are equal in magnitude and opposite in direction; on the other hand, it has a different spanwise velocity component along the foil span and it is at an angle to the incoming velocity at other positions of the cavity interface. In summary, the reentrant jet is three-dimensional at the vapor–liquid interface, which points to the centerline of the cavity, continuously moves toward the hydrofoil LE under the adverse pressure gradient [Fig. 7(a)], and finally cuts off a small part in the middle of the sheet vaporous cavity [Fig. 7(b)].

A cross section is established at $x = 0.25c$ in Fig. 13 to study the dependence of the vaporous cavity dynamics on the side-entrant jet. Figure 14 shows the velocity and pressure distributions over the surface-piercing hydrofoil at instant II. Figure 14(b) depicts that the pressure outside the vaporous cavity is larger than that inside the cavity. This adverse pressure gradient could generate the side-entrant jets, which are illustrated at the hydrofoil SS in Fig. 14(a). These two side-entrant jets are in opposite directions with strong spanwise components, and they collide in the midspan of the hydrofoil and then produce a velocity component perpendicular to the suction surface, causing the cutoff cavity to roll up, followed by a U-shaped shedding together with a concave residual cavity in Fig. 11(c).

In addition, there is a pressure difference at the hydrofoil tip since the pressure at the hydrofoil pressure side (PS) is larger than that at the hydrofoil SS. Therefore, the fluid is pushed across the hydrofoil tip from PS to SS, forming a crossflow at the hydrofoil tip. This would further make the pressure at the hydrofoil tip very low, resulting in a vaporous tip–vortex.

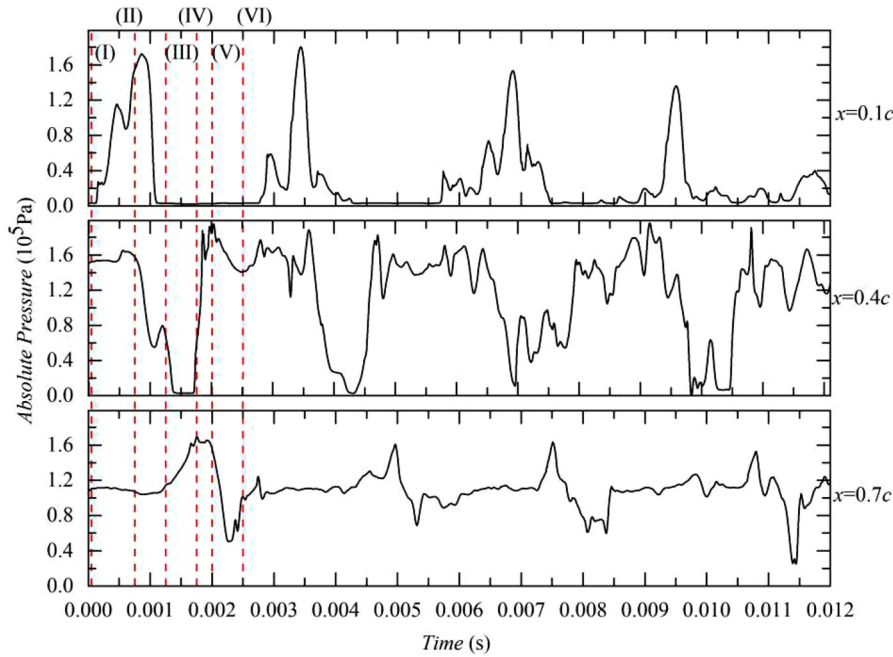
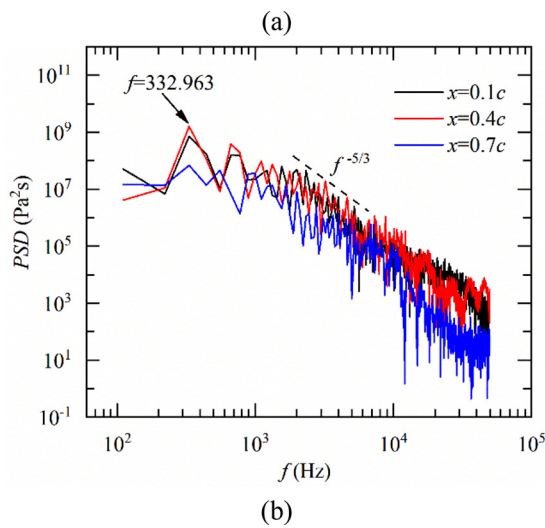


FIG. 10. (a) Pressure variation with time and (b) power spectral density (PSD) at three monitoring points, that is, $x/c = 0.1$, $x/c = 0.4$, $x/c = 0.7$.



C. Cavitation-vortex interaction

To analyze the cavity shedding behaviors, Q -criterion^{64,66} is adopted to visualize the vortex structures with the definition in Eq. (27), where Ω_{ij} indicates the vorticity tensor, and S_{ij} represents the rate of the strain tensor. Note that the Q calculated here only represents the resolved part, rather than the real Q . Although the resolved Q is much smaller than the real Q , regions with a high Q are found in regions of high macroscopic Q . Therefore, the resolved Q can still well identify the vortex structure

$$Q = \frac{1}{2} (\|\Omega_{ij}\|^2 - \|S_{ij}\|^2). \tag{27}$$

Figure 15 shows comparisons of cavitation patterns, vortex structures, and vorticity in the Z direction during one typical cycle. The isosurface of $\alpha_v = 0.1$ is used to visualize the cavity patterns on the left column, the isosurface of $Q = 100$ is used to identify vortex structures in the middle column, and the vorticity contour is shown at the XY plane with $z = -0.025$ m (i.e., the midspan). As shown in Fig. 15, the cavitating vortices mainly include a horseshoe vortex and tip-vortex structures. As mentioned in Sec. IV B, the crossflow at the hydrofoil tip is driven by the pressure gradient around the hydrofoil tip, and thus, tip-vortex structures are generated. In Fig. 15(a), the vortex structures are relatively stable when the vaporous cavitation is laid on the hydrofoil SS. Subsequently, a

Downloaded from http://pubs.aip.org/aip/pof/article-pdf/doi/10.1063/5.0123381/16602354/123314_1_online.pdf

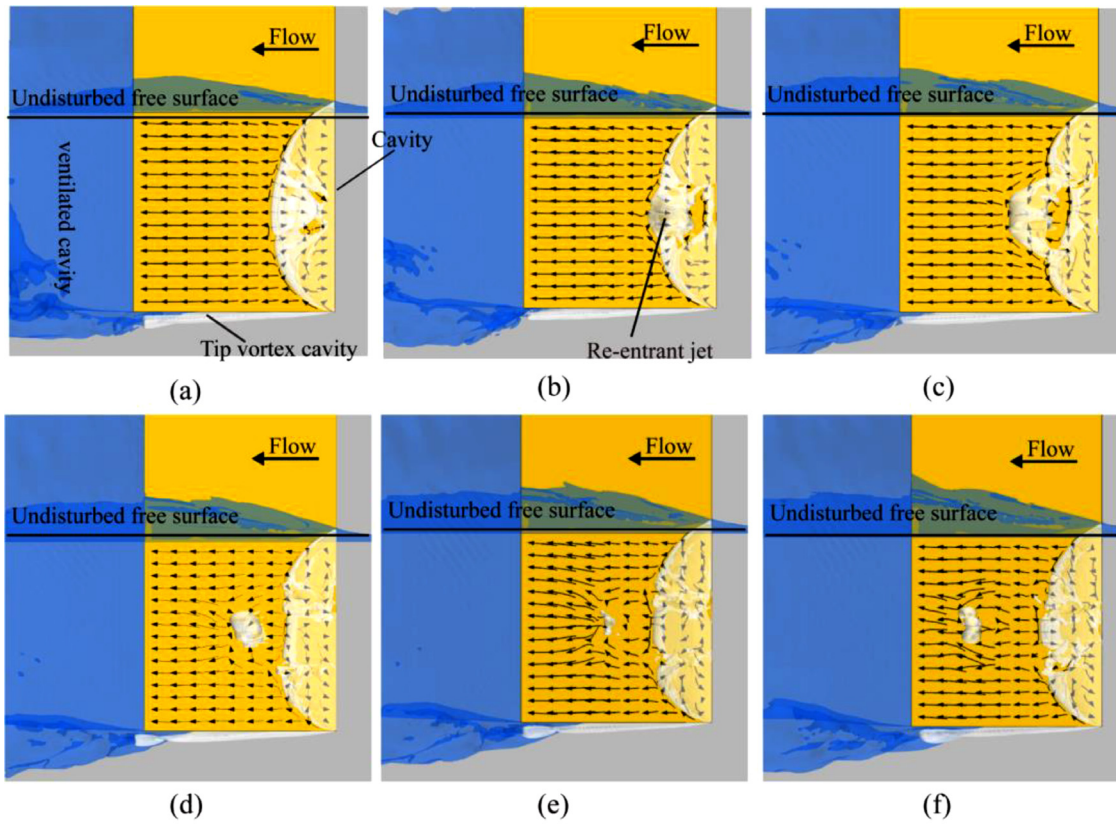


FIG. 11. Velocity distribution overlaid with the cavitation patterns during one typical cycle, where the vaporous cavity is identified with the $\alpha_v = 0.1$ isosurface in white color, and the ventilated cavity is visualized by the $\alpha_g = 0.5$ isosurface in blue color. (a)–(f) corresponds to instant I–VI in Fig. 6.

horseshoe vortex is formed with very complex coherent structures in Fig. 15(b). During Figs. 15(b)–15(f), the shed horseshoe vortex is rolled up and convected downstream toward the hydrofoil TE. The results suggest that the development of vortex structures is strongly associated with the cavity movement; therefore, the

cavitating vortices around the hydrofoil have the same evolution frequency as the cavitation evolution.

The vorticity transport equation^{18,24,64,67,68} is adopted to better understand the interaction mechanism between the turbulent vortex and the vaporous cavitation around the surface-piercing hydrofoil.

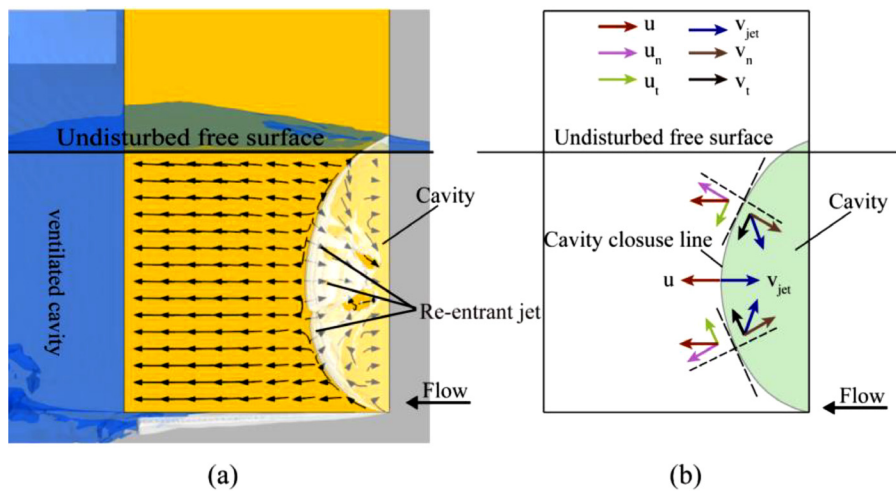


FIG. 12. Interpretation of the reentrant jet at instant I. (a) Simulated result, (b) the velocity reflection at the cavity closure line, which leads to three-dimensionality of the reentrant jet.

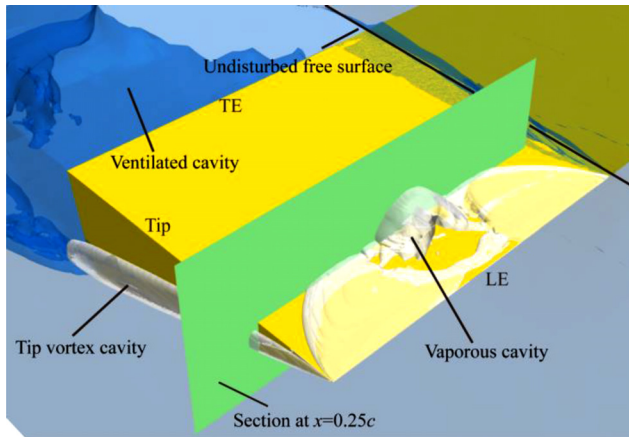


FIG. 13. Schematic diagram of the cross-section at $x = 0.25c$.

Note that the vorticity calculated here only represents the resolved part of the real vorticity

$$\frac{D\omega}{Dt} = (\omega \cdot \nabla)\mathbf{u} - \omega(\nabla \cdot \mathbf{u}) + \frac{1}{\rho_m^2}(\nabla\rho_m \times \nabla p) + (\nu_m + \nu_t)\nabla^2\omega. \quad (28)$$

In Eq. (28), ω is the vorticity. The first term on the right-hand side (RHS) denotes the vortex stretching term, which indicates the vorticity change caused by the velocity gradients.⁶⁹ The second term on the RHS denotes the vortex dilatation term, indicating how much the fluid compressibility affects the vorticity,⁷⁰ which is mainly caused by the fluid volume changes. The third term is the baroclinic torque term, and it is caused by the misalignment between the pressure gradient and the density gradient in a multiphase flow.^{71,72} The fourth term is the rate of vorticity change caused by the viscous diffusion,⁷³ which is significantly smaller than the other three terms and thus does not need to be considered in high Reynolds number flows. Therefore, the first three terms are discussed extensively in this study, that is, vortex dilatation, vortex stretching, and baroclinic torque.

To reveal the interaction mechanism between the vaporous cavitation and turbulent vortex, we select the midspan plane (i.e., at the XY plane $z = -0.025$ m) to illustrate the distributions of various terms in Eq. (28) along the Z direction, and the corresponding expressions are as follows:

$$[(\omega \cdot \nabla)\mathbf{u}]_z = \omega_x \frac{\partial u_z}{\partial x} + \omega_y \frac{\partial u_z}{\partial y} + \omega_z \frac{\partial u_z}{\partial z}, \quad (29)$$

$$[\omega(\nabla \cdot \mathbf{u})]_z = \omega_z \left(\frac{\partial u_x}{\partial x} + \frac{\partial u_y}{\partial y} + \frac{\partial u_z}{\partial z} \right), \quad (30)$$

$$\left[\frac{1}{\rho_m^2}(\nabla\rho_m \times \nabla p) \right]_z = \frac{1}{\rho_m^2} \left(\frac{\partial \rho_m}{\partial y} \cdot \frac{\partial p}{\partial x} - \frac{\partial \rho_m}{\partial x} \cdot \frac{\partial p}{\partial y} \right), \quad (31)$$

$$\omega_x = \frac{\partial u_z}{\partial y} - \frac{\partial u_y}{\partial z}, \quad \omega_y = \frac{\partial u_x}{\partial z} - \frac{\partial u_z}{\partial x}, \quad \omega_z = \frac{\partial u_y}{\partial x} - \frac{\partial u_x}{\partial y}. \quad (32)$$

Figure 16 shows the vortex stretching contours at the XY plane with $z = -0.025$ m, and the black dashed line shows the vaporous cavity with the isosurface of $\alpha_v = 0.1$, indicating the instantaneous cavity morphology. According to Eq. (28), the vortex stretching term has some connection with the velocity gradient. In Fig. 16, the vortex stretching is very significant during the unstable evolution of the vaporous cavitation, and it is primarily distributed near the hydrofoil SS and the cavity interface where both velocity gradients and pressure gradients change dramatically. In Figs. 16(a)–16(c), the cavity at the midspan is rolled up owing to the reentrant jet, presenting a convex shape, and it breaks into a cloud cavity in Fig. 16(d). This affects the velocity distribution around the cavity and causes obvious vortex stretching near the interface of vaporous cavitation and the hydrofoil SS. In Figs. 16(e) and 16(f), the cavitation is detached from the hydrofoil and it moves downstream through the mainstream. The shedding vapor cloud shrinks and expands, leading to a significant change in the velocity gradient at the hydrofoil wall near the vapor cloud, which in turn leads to a large vortex stretching region there.

Figure 17 shows the vortex dilatation distribution at the XY plane during a cavity shedding cycle. The vortex dilation is positively correlated with the velocity divergence ($\nabla \cdot \mathbf{u}$) and it is zero in the flow without cavitation, while it is a major contributor to the vorticity production in the cavitating flow. The vortex dilation is mainly gathered around the cavity interface, where the mixture density is variable and the multiphase flow is compressible, as depicted in Fig. 17.

The vortex baroclinic torque is illustrated in Fig. 18 at the hydrofoil midspan. The baroclinic torque is very significant near the cavity interface during the unstable evolution of the vaporous cavities since the pressure gradient is not parallel to the density gradient in the cavitating flow.⁵⁹ Note that the vortex dilatation is of the same order of magnitude as the baroclinic torque, indicating that the fluid compressibility and baroclinicity contribute equally to the vorticity generation in the cavitating flow.

Next, from the perspective of the inherent properties of the cavitating flow, the dimensionless operation is performed in Eq. (28).

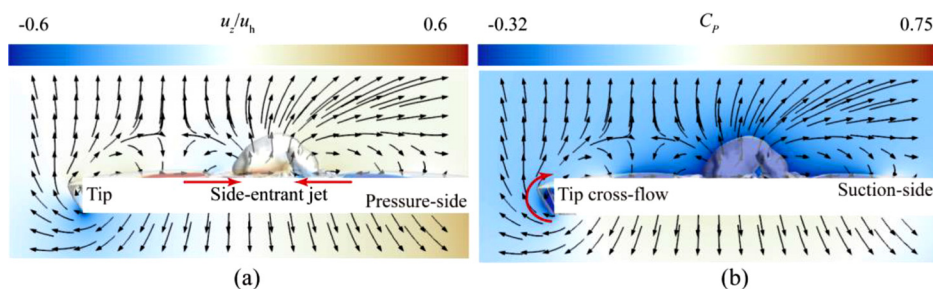


FIG. 14. Velocity and pressure distributions at instant II. (a) Velocity field, (b) pressure distribution (cross section at $x = 0.25c$).

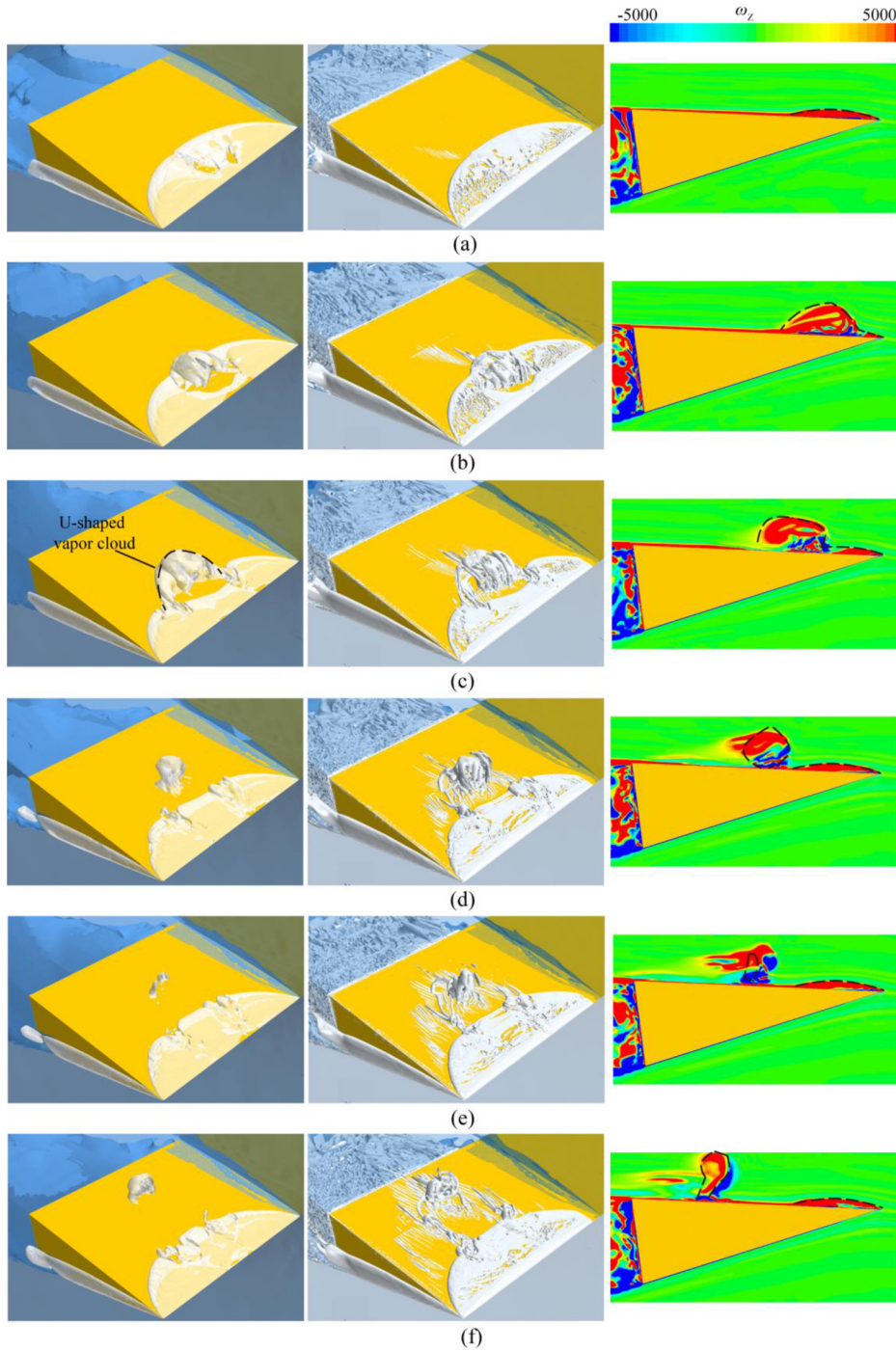


FIG. 15. Comparison of the cavitation patterns (left), vortex structures (middle), and vorticity in the Z direction (right) during one typical cycle. (a)–(f) corresponds to instant I–VI in Fig. 6.

The continuity equation can be expressed as

$$\frac{D\rho_m}{Dt} + \rho_m \nabla \cdot \mathbf{u} = 0. \tag{33}$$

Since the vorticity vector is defined as $\boldsymbol{\omega} = \nabla \times \mathbf{u}$, the vortex dilatation term $\boldsymbol{\omega}(\nabla \cdot \mathbf{u})$ is derived as follows:

$$-\boldsymbol{\omega}(\nabla \cdot \mathbf{u}) = \left(\frac{1}{\rho_m} \frac{D\rho_m}{Dt} \right) \boldsymbol{\omega}. \tag{34}$$

Then, Eq. (28) is modified as

$$\frac{D\boldsymbol{\omega}}{Dt} = (\boldsymbol{\omega} \cdot \nabla) \mathbf{u} + \left(\frac{1}{\rho_m} \frac{D\rho_m}{Dt} \right) \boldsymbol{\omega} + \frac{\nabla \rho_m \times \nabla p}{\rho_m^2} + (\nu_m + \nu_t) \nabla^2 \boldsymbol{\omega}. \tag{35}$$

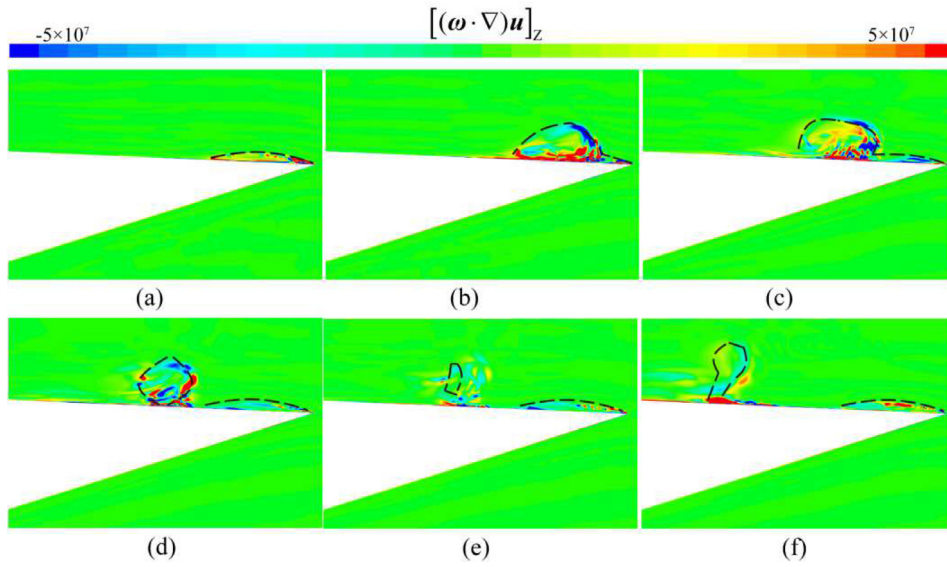


FIG. 16. Vortex stretching contours at the XY plane with $z = -0.025$ m, where the black dashed line represents the vapor cavity. (a)–(f) corresponds to instant I–VI in Fig. 6.

By defining the dimensionless parameters, $\omega' = \omega L_c / u_h$, $t' = t / t_{ref}$, $\mathbf{u}' = \mathbf{u} / u_h$, $\rho' = \rho_m / \rho_l$, $p' = p / p_\infty$, $\nu' = (\nu_m + \nu_l) / \nu_l$, where t_{ref} is the characteristic time, u_h is the hydrofoil velocity, and L_c is characteristic length with the value of $L_c = c$. Therefore, the dimensionless vorticity transport equation⁷⁴ can be obtained

$$\frac{D\omega'}{Dt'} = \frac{1}{St} (\omega' \cdot \nabla) \mathbf{u}' + \left(\frac{1}{\rho'} \frac{D\rho'}{Dt'} \right) \omega' + \frac{Eu}{St} \frac{\nabla \rho' \times \nabla p'}{(\rho')^2} + \frac{\nu'}{Re \cdot St} \nabla^2 \omega'. \quad (36)$$

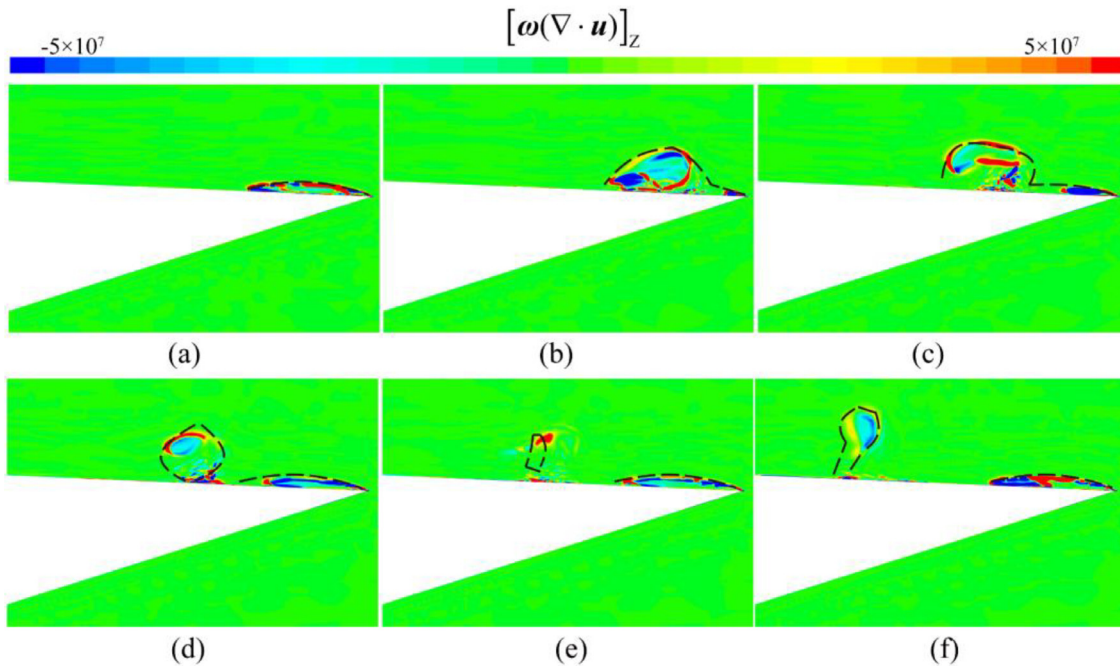


FIG. 17. Vortex dilatation contours at the XY plane with $z = -0.025$ m. (a)–(f) corresponds to instant I–VI in Fig. 6.

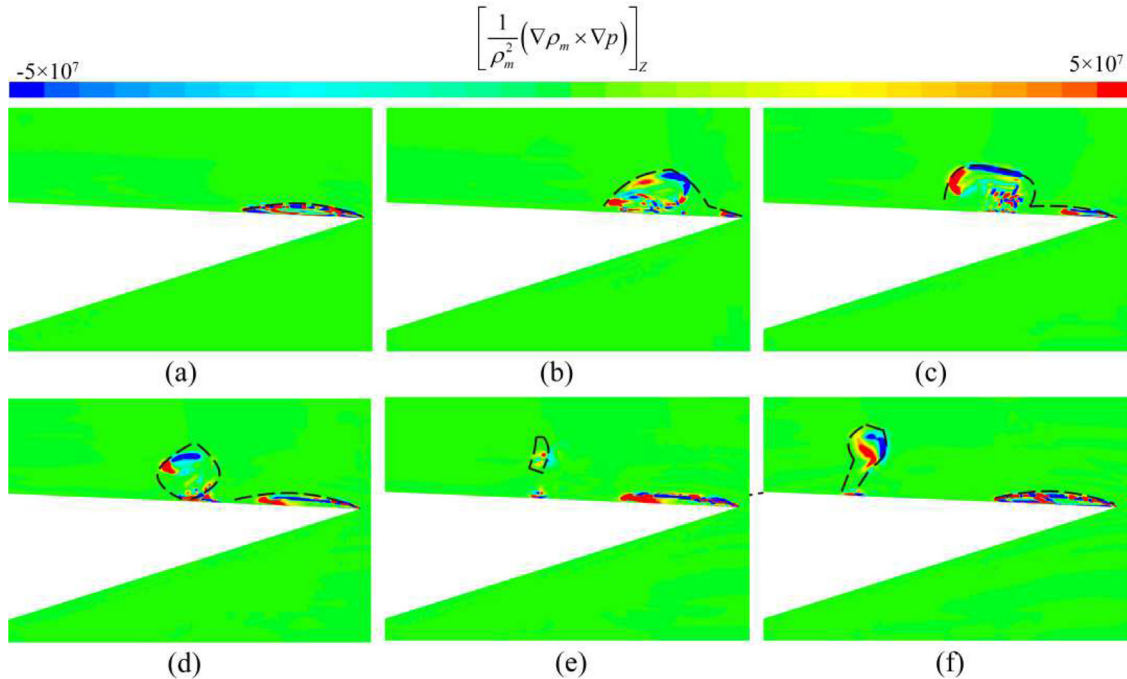


FIG. 18. Vortex baroclinic torque contours at the XY plane with $z = -0.025$ m. (a)–(f) corresponds to instant I–VI in Fig. 6.

St is Strouhal number with the definition as $St = L_c / (u_h t_{ref}) = 0.67$, which agrees well with the St value based on the simulated results. Eu is Euler number with the definition as $Eu = p_\infty / (\rho_l u_h^2) = 0.16$, and Re is Reynolds number with the definition as $Re = u_h L_c / \nu_l = 1.25 \times 10^6$.

The dimensionless vorticity transport equation in Eq. (36) indicates that the vorticity stretching is governed by St and it is associated with the unsteadiness of the cavitating vortical flow. The baroclinic torque term is dominated by St and Eu, and it also depends on the gradient of density and pressure. The vortex dilatation term is associated with the mixture density and vorticity. The viscous diffusion term depends on the St and Re, which has the smallest value and can be ignored since the Reynolds number is very high.

V. CONCLUSIONS

Unsteady cavitating flow over a surface-piercing plate hydrofoil is numerically investigated by utilizing LES and the Schnerr–Sauer cavitation model. Some fundamental mechanisms, such as the cavitation shedding dynamics, the three-dimensional effect of the reentrant jet, and cavitation–vortex interaction, are analyzed and summarized.

(1) Numerical simulations can capture the cavity features, including aerated base ventilation at the hydrofoil TE, vaporous cavitation at the hydrofoil SS, and tip–vortex cavitation. Specifically, the vaporous cavity behaviors include cavity development, cutoff, and collapse. It is interestingly observed that the tip–vortex cavitation does not intersect with the aerated base ventilation aft of the hydrofoil TE, and the free surface acts as a thin “seal” layer without gas ventilation.

- (2) A U-shaped vapor cloud shedding is coupled with horseshoe vortices during the unsteady cavitation evolution. This irregular shedding is induced by the collision between the radially diverging reentrant jet and the cavity closure line, and the reentrant jet has an obvious three-dimensional effect due to the velocity reflection at the vapor–liquid interface.
- (3) The cavitation–vortex interactions are evaluated by using the vorticity transport equation and demonstrate three major contributors, that is, baroclinic torque, vortex stretching, and vortex dilatation. The vortex stretching is related to cavity development, and the vortex dilatation and baroclinic torque terms are primarily focused upon the vaporous cavity region, especially at the liquid–vapor interface.

ACKNOWLEDGMENTS

The authors would like to acknowledge gratefully the National Natural Science Foundation of China (Grant Nos. 52006232 and 12122214).

AUTHOR DECLARATIONS

Conflict of Interest

The authors have no conflicts to disclose.

Author Contributions

Yuchang Zhi: Investigation (lead); Writing – original draft (lead). Renfang Huang: Conceptualization (lead); Funding acquisition

Downloaded from http://pubs.aip.org/aip/pof/article-pdf/doi/10.1063/5.0123381/16602354/123314_1_online.pdf

(equal); Supervision (lead); Writing – review & editing (lead). **Rundi Qiu:** Investigation (supporting). **Yiwei Wang:** Funding acquisition (equal); Resources (equal); Supervision (equal). **Chenguang Huang:** Resources (equal); Supervision (supporting).

DATA AVAILABILITY

The data that support the findings of this study are available from the corresponding author upon reasonable request.

NOMENCLATURE

AR_h	Immersed aspect ratio
C_L	Lift coefficient
\bar{C}_L	Mean lift coefficient
C_p	Pressure coefficient
C_s	WALE model parameter with the default value of 0.5
c	Chord length (m)
d	The shortest distance to the solid wall
Eu	Euler number
F_c	Frequency resolution, $F_c = 1/\Delta T/L = 55.56$ Hz
F_s	Safety factor
Fr_h	Depth Froude number
f_1, f_2	Parameters of the damping model
h	Tip immersed depth (m)
L_c	Characteristic length, $=c$
L	The number of samples, $=1800$
\dot{m}^+	Evaporation rate ($\text{kg m}^{-3} \text{s}^{-1}$)
\dot{m}^-	Condensation rate ($\text{kg m}^{-3} \text{s}^{-1}$)
N_1, N_2, N_3	Number of cells for the coarse, medium, and fine meshes
N_b	Number density of bubbles
n_d	Parameters of the damping model
P_{atm}	Standard atmospheric pressure
p	Pressure (Pa)
p_{out}	Static pressure at the outlet (Pa)
p_v	Saturated vapor pressure (Pa)
R_b	Bubble radius
Re	Reynolds number
r	Mesh refinement ratio
S	Hydrofoil span (m)
S_{ij}	The rate of the strain tensor
\bar{S}_{ij}	Strain rate tensor for the resolved quantities
St	Strouhal number
t_{ref}	Characteristic time (s)
u	Velocity (m s^{-1})
u_h	Hydrofoil velocity
V	The volume of the cell
V_{cav}	Total vapor volume
V_i	The volume of the i th cell.
V_n	Volume of n th phase within the cell (m^{-3}), $n = 1-3$
w	Vertical velocity component
x_{ed}	The end point for wave damping (boundary)
x_{sd}	The starting point for wave damping (propagation in the x -direction)
α	Volume fraction
α_0	Hydrofoil yaw angle (deg)

α_{vi}	The vapor volume fraction (α_v) of the i th grid cell
γ	The order of convergence
ΔT	The sampling interval, $= 1 \times 10^{-5}$ s
Δ_s	Mixing length of the SGS model
Δt	Time step
κ	von Karman constant
μ	Dynamic viscosity (Pa s)
μ_t	SGS turbulent viscosity
ν	Kinematic viscosity ($\text{m}^2 \text{s}^{-1}$)
ρ	Density (kg m^{-3})
σ	Vaporous cavitation number
τ_{ij}	Sub-grid-scale (SGS) stress
τ_{kk}	Isotropic part of the sub-grid-scale (SGS) stress
ω	Vorticity (s^{-2})
Ω_{ij}	Vorticity tensor

Subscripts

g	air phase
i, j, k	directions of the Cartesian coordinates
l	liquid phase
v	vapor phase
m	mixture component
out	outlet
∞	reference

REFERENCES

- Huang, R. Qiu, Y. Zhi, and Y. Wang, "Investigations into the ventilated cavities around a surface-piercing hydrofoil at high Froude numbers," *Phys. Fluids* **34**(4), 043304 (2022).
- M. S. Plesset and A. Prosperetti, "Bubble dynamics and cavitation," *Annu. Rev. Fluid Mech.* **9**(1), 145–185 (1977).
- M. Dular, B. Bachert, B. Stoffel, and B. Širok, "Relationship between cavitation structures and cavitation damage," *Wear* **257**(11), 1176–1184 (2004).
- Y. Zhi, Z. Zhang, R. Huang, R. Qiu, and Y. Wang, "Numerical investigations into supercavitating flows and hydrodynamic characteristics of a heaving hydrofoil," *Mod. Phys. Lett. B* **36**, 2150605 (2022).
- B. Stutz and J. Reboud, "Experiments on unsteady cavitation," *Exp. Fluids* **22**(3), 191–198 (1997).
- N. Lu, R. E. Bensow, and G. Bark, "Les of unsteady cavitation on the delft twisted foil," *J. Hydrodyn.* **22**(1), 742–749 (2010).
- B. Huang, S. Qiu, X. Li, Q. Wu, and G. Wang, "A review of transient flow structure and unsteady mechanism of cavitating flow," *J. Hydrodyn.* **31**(3), 429–444 (2019).
- J. B. Leroux, J. A. Astolfi, and J. Y. Billard, "An experimental study of unsteady partial cavitation," *J. Fluids Eng.* **126**(1), 94–101 (2004).
- Y. Liu, B. Huang, H. Zhang, Q. Wu, and G. Wang, "Experimental investigation into fluid-structure interaction of cavitating flow," *Phys. Fluids* **33**(9), 093307 (2021).
- B. Ji, X. Luo, R. E. Arndt, and Y. Wu, "Numerical simulation of three dimensional cavitation shedding dynamics with special emphasis on cavitation-vortex interaction," *Ocean Eng.* **87**, 64–77 (2014).
- B. Ji, X. Luo, R. E. Arndt, X. Peng, and Y. Wu, "Large eddy simulation and theoretical investigations of the transient cavitating vortical flow structure around a NACA66 hydrofoil," *Int. J. Multiphase Flow* **68**, 121–134 (2015).
- E. J. Foeth, C. Van Doorne, T. Van Terwisga, and B. Wieneke, "Time resolved PIV and flow visualization of 3D sheet cavitation," *Exp. Fluids* **40**(4), 503–513 (2006).
- E. J. Foeth, T. van Terwisga, and C. van Doorne, "On the collapse structure of an attached cavity on a three-dimensional hydrofoil," *J. Fluids Eng.* **130**(7), 071303 (2008).

- ¹⁴D. D. Lange and G. D. Bruin, "Sheet cavitation and cloud cavitation, re-entrant jet and three-dimensionality," *Appl. Sci. Res.* **58**(1), 91–114 (1997).
- ¹⁵X. Peng, B. Ji, Y. Cao, L. Xu, G. Zhang, X. Luo, and X. Long, "Combined experimental observation and numerical simulation of the cloud cavitation with u-type flow structures on hydrofoils," *Int. J. Multiphase Flow* **79**, 10–22 (2016).
- ¹⁶Y. Kawanami, H. Kato, H. Yamaguchi, M. Tanimura, and Y. Tagaya, "Mechanism and control of cloud cavitation," *J. Fluids Eng.* **119**, 788 (1997).
- ¹⁷A. Ducoin, B. Huang, and Y. L. Young, "Numerical modeling of unsteady cavitating flows around a stationary hydrofoil," *Int. J. Rotating Mach.* **2012**, 1.
- ¹⁸B. Huang, Y. Zhao, and G. Wang, "Large eddy simulation of turbulent vortex-cavitation interactions in transient sheet/cloud cavitating flows," *Comput. Fluids* **92**, 113–124 (2014).
- ¹⁹B. Huang, A. Ducoin, and Y. L. Young, "Physical and numerical investigation of cavitating flows around a pitching hydrofoil," *Phys. Fluids* **25**(10), 102109 (2013).
- ²⁰H. Cheng, X. Bai, X. Long, B. Ji, X. Peng, and M. Farhat, "Large eddy simulation of the tip-leakage cavitating flow with an insight on how cavitation influences vorticity and turbulence," *Appl. Math. Model.* **77**, 788–809 (2020).
- ²¹B. Tian, J. Chen, X. Zhao, M. Zhang, and B. Huang, "Numerical analysis of interaction between turbulent structures and transient sheet/cloud cavitation," *Phys. Fluids* **34**(4), 047116 (2022).
- ²²X. Long, H. Cheng, B. Ji, R. E. Arndt, and X. Peng, "Large eddy simulation and Euler–Lagrangian coupling investigation of the transient cavitating turbulent flow around a twisted hydrofoil," *Int. J. Multiphase Flow* **100**, 41–56 (2018).
- ²³X. Luo, B. Ji, X. Peng, H. Xu, and M. Nishi, "Numerical simulation of cavity shedding from a three-dimensional twisted hydrofoil and induced pressure fluctuation by large-eddy simulation," *J. Fluids Eng.* **134**(4), 041202 (2012).
- ²⁴B. Ji, X. Luo, X. Peng, and Y. Wu, "Three-dimensional large eddy simulation and vorticity analysis of unsteady cavitating flow around a twisted hydrofoil," *J. Hydrodyn.* **25**(4), 510–519 (2013).
- ²⁵B. Ji, X. Luo, Y. Wu, X. Peng, and Y. Duan, "Numerical analysis of unsteady cavitating turbulent flow and shedding horse-shoe vortex structure around a twisted hydrofoil," *Int. J. Multiphase Flow* **51**, 33–43 (2013).
- ²⁶J. Decaix and E. Goncalves, "Investigation of three-dimensional effects on a cavitating venturi flow," *Int. J. Heat Fluid Flow* **44**, 576–595 (2013).
- ²⁷T. Yin, G. Pavesi, J. Pei, and S. Yuan, "Numerical investigation of unsteady cavitation around a twisted hydrofoil," *Int. J. Multiphase Flow* **135**, 103506 (2021).
- ²⁸C. Xu, J. Huang, Y. Wang, X. Wu, C. Huang, and X. Wu, "Supercavitating flow around high-speed underwater projectile near free surface induced by air entrainment," *AIP Adv.* **8**(3), 035016 (2018).
- ²⁹Y. Wang, C. Xu, X. Wu, C. Huang, and X. Wu, "Ventilated cloud cavitating flow around a blunt body close to the free surface," *Phys. Rev. Fluids* **2**(8), 084303 (2017).
- ³⁰O. M. Faltinsen and Y. A. Semenov, "The effect of gravity and cavitation on a hydrofoil near the free surface," *J. Fluid Mech.* **597**, 371–394 (2008).
- ³¹C. Xu, Y. Wang, C. Huang, C. Yu, and J. Huang, "Cloud cavitating flow that surrounds a vertical hydrofoil near the free surface," *J. Fluids Eng.* **139**(10), 101302 (2017).
- ³²Y. Wang, X. Wu, and C. Huang, "Ventilated partial cavitating flow around a blunt body near the free surface," in 16th International Symposium on Transport Phenomena and Dynamics of Rotating Machinery, 2016.
- ³³Y. Wang, X. Wu, C. Huang, and X. Wu, "Unsteady characteristics of cloud cavitating flow near the free surface around an axisymmetric projectile," *Int. J. Multiphase Flow* **85**, 48–56 (2016).
- ³⁴C. Xu, J. Huang, C. Yu, Y. Wang, C. Huang, and B. C. Khoo, "Free surface and near-wall effects on the cloud cavitating flow over an axisymmetric projectile," *Ocean Eng.* **238**, 109682 (2021).
- ³⁵C. Xu, Y. Wang, C. Huang, C. Yu, and J. Huang, "Analysis of near-wall effect on cloud cavitating flow that surrounds an axisymmetric projectile using large eddy simulation with Cartesian cut-cell mesh method," *Eur. J. Mech. B* **67**, 15–24 (2018).
- ³⁶C. Xu, Y. Wang, C. Huang, J. Huang, and C. Yu, "The effect of free surface on cloud cavitating flow around a blunt body," *J. Hydrodyn.* **29**(6), 979–986 (2017).
- ³⁷Z. Li, C. Liu, D. Wan, and C. Hu, "High-fidelity simulation of a hydraulic jump around a surface-piercing hydrofoil," *Phys. Fluids* **33**(12), 123304 (2021).
- ³⁸Y. Hu, C. Liu, C. Hu, and D. Wan, "Numerical investigation of flow structure and air entrainment of breaking bow wave generated by a rectangular plate," *Phys. Fluids* **33**(12), 122113 (2021).
- ³⁹S. Chen, W. Zhao, and D. Wan, "On the scattering of focused wave by a finite surface-piercing circular cylinder: A numerical investigation," *Phys. Fluids* **34**(3), 035132 (2022).
- ⁴⁰S. Chen, W. Zhao, and D. Wan, "Turbulent structures and characteristics of flows past a vertical surface-piercing finite circular cylinder," *Phys. Fluids* **34**(1), 015115 (2022).
- ⁴¹R. S. Rothblum, D. A. Mayer, and G. M. Wilburn, "Ventilation, cavitation and other characteristics of high speed surface-piercing struts," Technical Report No. 3023, Department of the Navy, Naval Ship Research and Development Center, Washington, DC, 1969.
- ⁴²R. S. Rothblum, "Investigation of methods of delaying or controlling ventilation on surface piercing struts," Ph.D. thesis (University of Leeds, 1977).
- ⁴³R. L. Waid, *Experimental Investigation of the Ventilation of Vertical Surface-Piercing Struts in the Presence of Cavitation* (Naval Ship Research and Development Center, 1968).
- ⁴⁴C. M. Harwood, K. A. Brucker, F. Miguel, Y. L. Young, and S. L. Ceccio, "Experimental and numerical investigation of ventilation inception and wash-out mechanisms of a surface-piercing hydrofoil," in 30th Symposium on Naval Hydrodynamics, Hobart, Tasmania, Australia, 2014.
- ⁴⁵C. M. Harwood, Y. L. Young, and S. L. Ceccio, "Ventilated cavities on a surface-piercing hydrofoil at moderate Froude numbers: Cavity formation, elimination and stability," *J. Fluid Mech.* **800**, 5–56 (2016).
- ⁴⁶Y. Zhi, J. Zhan, R. Huang, R. Qiu, and Y. Wang, "Numerical investigations into the ventilation elimination mechanism of a surface-piercing hydrofoil," *Ocean Eng.* **243**, 110225 (2022).
- ⁴⁷Y. Wang, C. Huang, T. Du, R. Huang, Y. Zhi, Y. Wang, Z. Xiao, and Z. Bian, "Research on ventilation and supercavitation mechanism of high-speed surface-piercing hydrofoil," *Phys. Fluids* **34**(2), 023316 (2022).
- ⁴⁸S. Brizzolara and D. Villa, "Three phases RANSE calculations for surface-piercing super-cavitating hydrofoils," in 8th International Symposium on Cavitation CAV2012, Singapore, 2012.
- ⁴⁹B. Ji, J. Wang, X. Luo, K. Miyagawa, L. Z. Xiao, X. Long, and Y. Tsujimoto, "Numerical simulation of cavitation surge and vortical flows in a diffuser with swirling flow," *J. Mech. Sci. Technol.* **30**(6), 2507–2514 (2016).
- ⁵⁰M. R. Pendar and E. Roohi, "Cavitation characteristics around a sphere: An LES investigation," *Int. J. Multiphase Flow* **98**, 1–23 (2018).
- ⁵¹R. Huang, T. Du, Y. Wang, and C. Huang, "Numerical investigations of the transient cavitating vortical flow structures over a flexible NACA66 hydrofoil," *J. Hydrodyn.* **32**(5), 865–878 (2020).
- ⁵²G. H. Schnerr and J. Sauer, "Physical and numerical modeling of unsteady cavitation dynamics," in Fourth International Conference on Multiphase Flow, New Orleans, USA, 2001.
- ⁵³T. Sun, Q. Xie, X. Li, and L. Zou, "Numerical investigation of the effects of free surface on tip-leakage vortex cavitation behaviors over a NACA0009 hydrofoil," *Int. J. Multiphase Flow* **141**, 103671 (2021).
- ⁵⁴Y. Liu, J. Long, Q. Wu, B. Huang, and G. Wang, "Data-driven modal decomposition of transient cavitating flow," *Phys. Fluids* **33**(11), 113316 (2021).
- ⁵⁵F. Nicoud and F. Ducros, "Subgrid-scale stress modelling based on the square of the velocity gradient tensor," *Flow, Turbul. Combust.* **62**(3), 183–200 (1999).
- ⁵⁶J. H. Kim, J. H. Choi, and K. Y. Kim, "Design optimization of a centrifugal compressor impeller using radial basis neural network method," in ASME Turbo Expo 2009: Power for Land, Sea, and Air, 2009.
- ⁵⁷T. Sun, S. Dong, Y. Liu, H. Huang, and G. Zhang, "Physical investigation of transient dynamic behaviors of cavitation-induced vibration over a flexible hydrofoil," *Phys. Fluids* **33**(11), 113303 (2021).
- ⁵⁸O. Coutier-Delgosha, J. Reboud, and Y. Delannoy, "Numerical simulation of the unsteady behaviour of cavitating flows," *Int. J. Numer. Methods Fluids* **42**(5), 527–548 (2003).
- ⁵⁹T. Sun, Y. Wei, L. Zou, Y. Jiang, C. Xu, and Z. Zong, "Numerical investigation on the unsteady cavitation shedding dynamics over a hydrofoil in thermo-sensitive fluid," *Int. J. Multiphase Flow* **111**, 82–100 (2019).

- ⁶⁰Y. Long, X. Long, B. Ji, W. Huai, and Z. Qian, "Verification and validation of URANS simulations of the turbulent cavitating flow around the hydrofoil," *J. Hydrodyn.* **29**(4), 610–620 (2017).
- ⁶¹T. S. Phillips and C. J. Roy, "Richardson extrapolation-based discretization uncertainty estimation for computational fluid dynamics," *J. Fluids Eng.* **136**(12), 121401 (2014).
- ⁶²Y. Saito, R. Takami, I. Nakamori, and T. Ikohagi, "Numerical analysis of unsteady behavior of cloud cavitation around a NACA0015 foil," *Comput. Mech.* **40**(1), 85–96 (2007).
- ⁶³Y. L. Young, C. M. Harwood, F. Miguel Montero, J. C. Ward, and S. L. Ceccio, "Ventilation of lifting bodies: Review of the physics and discussion of scaling effects," *Appl. Mech. Rev.* **69**(1), 010801 (2017).
- ⁶⁴P. K. Kundu, I. M. Cohen, and D. R. Dowling, *Fluid Mechanics* (Academic Press, 2015).
- ⁶⁵M. Dular, R. Bachert, C. Schaad, and B. Stoffel, "Investigation of a re-entrant jet reflection at an inclined cavity closure line," *Eur. J. Mech. B* **26**(5), 688–705 (2007).
- ⁶⁶J. C. R. Hunt, A. A. Wray, and P. Moin, "Eddies, streams, and convergence zones in turbulent flows," in *Proceedings of the 1988 Summer Program (Studying Turbulence Using Numerical Simulation Databases, 1988)*, pp. 193–208.
- ⁶⁷W. Ye, Y. Yi, and X. Luo, "Numerical modeling of unsteady cavitating flow over a hydrofoil with consideration of surface curvature," *Ocean Eng.* **205**, 107305 (2020).
- ⁶⁸X. Li, Y. Liu, Z. Zhu, P. Lin, and L. Li, "Boundary vorticity analysis and shedding dynamics of transient cavitation flow around a twisted hydrofoil," *J. Fluids Eng.* **143**(7), 071501 (2021).
- ⁶⁹X. Long, D. Zuo, H. Cheng, and B. Ji, "Large eddy simulation of the transient cavitating vortical flow in a jet pump with special emphasis on the unstable limited operation stage," *J. Hydrodyn.* **32**(2), 345–360 (2020).
- ⁷⁰Z. Li, Z. Qian, and B. Ji, "Transient cavitating flow structure and acoustic analysis of a hydrofoil with whale like wavy leading edge," *Appl. Math. Modell.* **85**, 60–88 (2020).
- ⁷¹Y. Long, C. Han, B. Ji, X. Long, and Y. Wang, "Verification and validation of large eddy simulations of turbulent cavitating flow around two marine propellers with emphasis on the skew angle effects," *Appl. Ocean Res.* **101**, 102167 (2020).
- ⁷²X. Zhao, H. Cheng, and B. Ji, "LES investigation of the cavitating hydrofoils with various wavy leading edges," *Ocean Eng.* **243**, 110331 (2022).
- ⁷³X. Long, H. Cheng, B. Ji, and R. E. A. Arndt, "Numerical investigation of attached cavitation shedding dynamics around the Clark-Y hydrofoil with the FBDCM and an integral method," *Ocean Eng.* **137**, 247–261 (2017).
- ⁷⁴M. Liu, L. Tan, and S. Cao, "Cavitation–vortex–turbulence interaction and one-dimensional model prediction of pressure for hydrofoil ALE15 by large eddy simulation," *J. Fluids Eng.* **141**(2), 021103 (2019).